Rayleigh Damping in the Free Troposphere

DAVID M. ROMPS

Department of Earth and Planetary Science, University of California, Berkeley, and Earth Sciences Division, Lawrence Berkeley National Laboratory, Berkeley, California

(Manuscript received 16 February 2013, in final form 24 October 2013)

ABSTRACT

This paper explores whether cumulus drag (i.e., the damping of winds by convective momentum transport) can be described by an effective Rayleigh drag (i.e., the damping of winds on a constant time scale). Analytical expressions are derived for the damping time scale and descent speed of wind profiles as caused by unorganized convection. Unlike Rayleigh drag, which has a constant damping time scale and zero descent speed, the theory predicts a damping time scale and a descent speed that both depend on the vertical wavelength of the wind profile. These results predict that short wavelengths damp faster and descend faster than long wavelengths, and these predictions are confirmed using large-eddy simulations. Both theory and simulations predict that the convective damping of large-scale circulations occurs on a time scale of $O(1–10)$ days for vertical wavelengths in the range of 2–10 km.

1. Introduction

For nearly 50 years, Rayleigh damping has been used in simplified models of atmospheric dynamics. The Matsuno–Gill model uses a Rayleigh damping, and authors have typically found the best match with observations using a damping time scale in the range of 1–10 days. For example, a brief survey of the literature finds Matsuno–Gill models used with damping time scales of 1.8 days (Matsuno 1966), 5 days (Chang 1977), 2.5 days (Gill 1980), ≥3 days (Chang and Lim 1982), 2–5 days (Neelin et al. 1987), 1.25 days (Seager 1991), 2 days (Yu and Neelin 1997), 10 days (Wu et al. 2000), 10–20 days (Lee et al. 2009), and 5 days (Sugiyama 2009). Another model of atmospheric dynamics that makes use of a Rayleigh damping is the weak pressure gradient (WPG) approximation (e.g., Romps 2012c). Damping time scales used with WPG include 0.5 days (Raymond and Zeng 2000), 4 and 10 days (Kuang 2008), 1–10 days (Blossey et al. 2009), 2.5 days (Kuang 2011), and 0.4 days (Romps 2012a). Furthermore, studies of the National Centers for Environmental Prediction–National Center for Atmospheric Research (NCEP–NCAR) and European Centre for Medium-Range Weather Forecasts (ECMWF) reanalyses conclude that the momentum budget of the Madden–Julian oscillation in those reanalyses can be closed by the addition of a damping time scale on the order of 2–10 days (Lin et al. 2005), and similarly for the Walker circulation with a damping time scale of 1–10 days over the warm pool (Lin et al. 2008).

Why have the majority of these papers found it efficacious to include a damping time scale in the range of 1–10 days? And what physical mechanism operating in the free troposphere could generate such a Rayleigh damping? In the early 1970s, Holton and Colton (1972) found evidence for damping of upper-tropospheric winds (with a time scale of 2 days) and concluded that momentum transport by moist convection must be responsible. Ever since, studies of the Matsuno–Gill models have justified their use of Rayleigh damping by alluding to convective momentum transport. Indeed, the accumulated evidence from a variety of studies points to a potentially significant role for convective momentum transport in the large-scale momentum budget (e.g., Houze 1973; Schneider and Lindzen 1977; Carr and Bretherton 2001; Yang et al. 2013). For example, Robe and Emanuel (2001) found a damping time scale of 0.5 days in their cloud-resolving simulation of radiative–convective equilibrium (RCE). In another study with a cloud-resolving model, Mapes and Wu (2001) found a damping rate of kinetic energy that ranged from -40% to -80% per centimeter of precipitation; for a rain rate between 1 and 4 m yr^{-1} (typical of the deeply convecting

Corresponding author address: David M. Romps, Department of Earth and Planetary Science, 377 McCone Hall, University of California, Berkeley, Berkeley, CA 94720.
E-mail: romps@berkeley.edu

DOI: 10.1175/JAS-D-13-062.1

tropics), this translates into a damping time scale for momentum between 1 and 14 days. Nevertheless, no theory has been developed to explain why convection should generate a Rayleigh damping on these time scales.

This paper explores the effect of moist convection on shear in a simple bulk-plume model and in large-eddy simulations. The focus here is on unorganized convection, as opposed to organized convection, which is known to interact with shear in such a way as to produce upgradient momentum transfer (e.g., LeMone 1983; Moncrieff 1992; Wu and Yanai 1994). The next section derives an analytical theory for the effect of unorganized convection on wind profiles using the bulk-plume equations. Although convective downdrafts can make a substantial contribution to mass fluxes (e.g., Johnson 1976; Jorgensen et al. 1985), they are neglected in this theory for simplicity. Following the derivation in section 2, section 3 tests the validity of this analytical theory by comparing it against the evolution of passive tracers in a large-eddy simulation of RCE. Section 4 repeats this analysis for simulations with sinusoidal wind profiles, and section 5 summarizes the findings and discusses the implications.

2. Theory

The bulk-plume equations for convective momentum transport can be written as

$$\partial_z M = (\varepsilon - \delta)M, \tag{1}$$

$$\rho\partial_t \boldsymbol{v} = \partial_z[M(\boldsymbol{v} - \boldsymbol{v}_c)], \quad \text{and} \tag{2}$$

$$\partial_z \boldsymbol{v}_c = \varepsilon(\boldsymbol{v} - \boldsymbol{v}_c) + \mathbf{F}/M, \tag{3}$$

where M is the convective mass flux (kg m^{-2} s^{-1}), ε is the fractional entrainment rate (m^{-1}), δ is the fractional detrainment rate (m^{-1}), $\boldsymbol{v}$ is the mean horizontal wind (m s^{-1}), $\boldsymbol{v}_c$ is the mean horizontal wind in the clouds (m s^{-1}), and $\mathbf{F}$ is the mean horizontal pressure gradient force (per volume of total air) of the environment on the clouds (N m^{-3}). These bulk-plume equations have been used in the literature for many decades: Eq. (2) traces back to Eq. (7) in Schneider and Lindzen (1976), and Eq. (3) traces back to Eq. (4) in Malkus (1952). A concise derivation of both is given by Romps (2012b). The starting point is to approximate the atmosphere as comprising two homogeneous constituents: cloud and environment. The derivation also assumes that clouds occupy a small fractional area and that the clouds adjust quickly to a steady state (Romps 2012b). In this limit of small fractional area for clouds, the environmental velocity is the same as the domain-averaged velocity $\boldsymbol{v}$. In the context of a general circulation model, we may think of $\boldsymbol{v}$ as the resolved horizontal velocity and $\boldsymbol{v}_c$ as the unresolved horizontal velocity within convective clouds.

Since it is not known how to parameterize the pressure gradient force between clouds and their environment, we will proceed with a simplifying ansatz: we will assume that $\mathbf{F} \propto M(\boldsymbol{v} - \boldsymbol{v}_c)$. This formulation assumes that the force on a cloud is proportional to the relative velocity of its environment and that the net force on all clouds scales like the total cloud mass flux (i.e., a constant force per cloud). The great benefit of this formulation is that the right-hand side of Eq. (3) can be written as $\varepsilon(\boldsymbol{v} - \boldsymbol{v}_c)$ for some effective entrainment rate ε that includes the effects of both entrainment and the pressure gradient force. Henceforth, we will drop the $\mathbf{F}/M$ term, which reduces the bulk-plume equations to those applicable to a passive tracer. Focusing on one component of the horizontal wind, Eqs. (1)–(3) can be written as (Romps 2012b)

$$\partial_t v(z) = \frac{M(z)}{\rho(z)}\left\{\partial_z v(z) - \delta(z)\int_{z_0}^{z} dz' \exp\left[-\int_{z'}^{z} dz''\varepsilon(z'')\right]\partial_{z'}v(z')\right\}, \tag{4}$$

where we have assumed that $v_c(z_0) = v(z_0)$. This equation gives the tendency of $v(z)$ as a function of $v(z')$ for all $z' \in [z_0, z]$.

For constant ε and δ, and for $(z - z_0)\varepsilon \gg 1$ (so that z_0 can be treated as $-\infty$), this simplifies to

$$\partial_t v(z) = \frac{M(z)}{\rho(z)}\left\{\partial_z v(z) - \delta\int_{-\infty}^{z} dz' \exp[-(z - z')\varepsilon]\partial_{z'}v(z')\right\}. \tag{5}$$

According to Eq. (5), an initial sinusoidal wind profile of wavenumber m evolves in time as

$$v = v_0 e^{-t/\tau}\cos[m(z - wt)], \tag{6}$$

where the ascent speed w and Rayleigh damping time scale τ are given by

$$w = -\frac{M}{\rho}\left(1 - \frac{\delta\varepsilon}{\varepsilon^2 + m^2}\right) \quad \text{and} \tag{7}$$

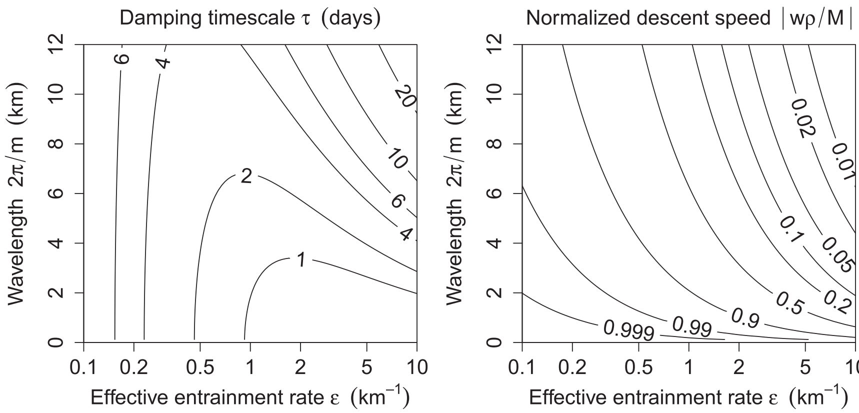

FIG. 1. (left) The damping time scale τ and (right) the normalized descent speed $|w\rho/M|$ for transient solutions as predicted by Eqs. (9) and (10) using $M/\rho = 1\,\mathrm{cm\,s^{-1}}$.

$$\tau = \frac{\rho}{M}\frac{\varepsilon^2 + m^2}{\delta m^2}. \tag{8}$$

Romps (2010) found that ε and δ are of similar magnitude for deep convection, which motivates making the approximation of $\varepsilon = \delta$. This approximation is evaluated in the following sections and is found to be satisfactory for our purposes. Therefore, we replace δ with ε in the expressions above to obtain

$$w = -\frac{M}{\rho}\frac{m^2}{\varepsilon^2 + m^2} \quad \text{and} \tag{9}$$

$$\tau = \frac{\rho}{M}\frac{\varepsilon^2 + m^2}{\varepsilon m^2}. \tag{10}$$

Equations (9) and (10) are two of the main new results: they give the descent and decay of unforced wind profiles as functions of vertical wavenumber and the convective entrainment rate. These expressions exhibit a rich dependence on ε and m, as shown in Fig. 1. It is of particular interest to note that, over a plausible range of fractional entrainment rates (i.e., within an order of magnitude of $1\,\mathrm{km^{-1}}$), the damping time scale is predicted to lie largely in the range of 1–10 days.

To aid in summarizing Fig. 1, it is helpful to consider Eqs. (9) and (10) in the limits of small and large wavelengths—that is, for small and large $\lambda = 2\pi/m$. For small wavelengths ($\lambda \ll 2\pi/\varepsilon$), the profile experiences strong descent ($|w| \approx M/\rho \approx 1\,\mathrm{cm\,s^{-1}}$) and strong damping ($\tau \approx \rho/M\varepsilon \approx 1$ day, assuming $\varepsilon \approx 1\,\mathrm{km^{-1}}$). For large wavelengths ($\lambda \gg 2\pi/\varepsilon$), the profile experiences weak descent ($|w| \ll M/\rho$) and weak damping ($\tau \gg \rho/M\varepsilon$). These results are summarized in Fig. 2.

Small and large wavelengths also differ in terms of the relative importance of damping and descent. To see how, note that $|w|\tau$ is the vertical distance a profile descends in the time it takes to damp by an e folding. Therefore, $|w|\tau m/2\pi$ is the number of wavelengths that the profile descends during an e folding. Using Eqs. (9) and (10), this expression simplifies, yielding

$$\text{Number of } \lambda \text{ descended in an } e\text{-folding} = \frac{1/\varepsilon}{\lambda}.$$

In other words, the ratio of λ and $1/\varepsilon$ indicates the relative strength of damping versus descent. Small-wavelength profiles descend many wavelengths with little damping, while large-wavelength profiles mostly damp in place. This is the result that one would get by assuming that the damping rate and descent speed do not depend on wavelength. Here, we see that the damping rate and descent speed do depend on the wavelength, but their ratio does not, which leads to the same conclusion of "small wavelengths descend, long wavelengths damp."

Furthermore, for large wavelengths, the damping can be approximated by a constant viscosity. For $\lambda \gg 2\pi/\varepsilon$, Eqs. (9) and (10) reduce to $w \approx 0$ and $\tau \approx \rho\varepsilon/Mm^2$, respectively. In this case, Eq. (6) is a solution to the diffusive

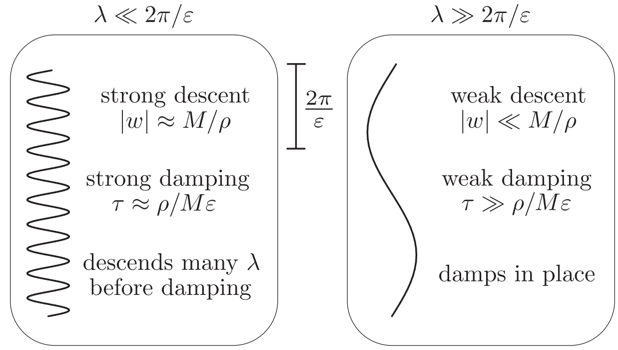

FIG. 2. The dependence of descent speed $|w|$ and damping time scale τ on the vertical wavelength λ of profiles.

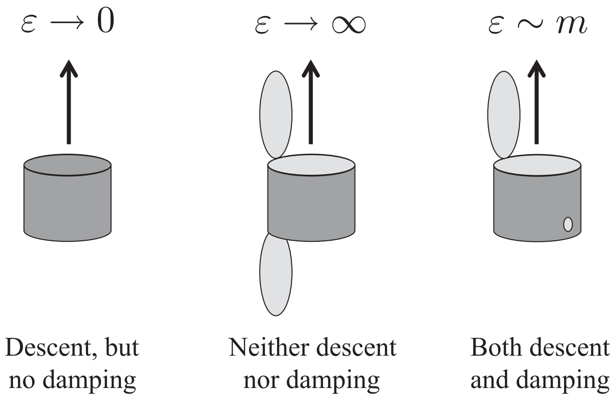

FIG. 3. The dependence of descent speed $|w|$ and damping time scale τ on the convective entrainment rate ε.

equation $\partial_t v = \nu \partial_z^2 v$, where $\nu = M/\rho\varepsilon$ is the effective kinematic viscosity. Using $\varepsilon = 1\,\mathrm{km}^{-1}$ and $M/\rho = 1$–$3\,\mathrm{cm\,s}^{-1}$, which is characteristic of the deeply convecting tropics, we find that $\nu = 10$–$30\,\mathrm{m}^2\,\mathrm{s}^{-1}$. Note that this viscosity is about one order of magnitude larger than estimates obtained for clear-air turbulence using radar (Wilson 2004) and radiosondes (Clayson and Kantha 2008).

Equations (9) and (10) also reveal an interesting dependence of w and τ on ε. For small entrainment rates ($\varepsilon \to 0$), profiles experience descent, but no damping, as discussed by Mapes and Wu (2001). This can be understood from the fact that a low-entrainment cloud exchanges very little mass with the environment as it rises. Such a cloud may be visualized as a closed canister rising through the atmosphere; its only impact on the environment is to cause compensating subsidence. This case, along with others, is depicted in Fig. 3. For large entrainment rates ($\varepsilon \to \infty$), profiles neither descend nor damp. This is a counterintuitive result: a cloud that is interacting strongly with its environment has no impact on the environmental profiles. This can be visualized as a canister that has been opened at the top and bottom allowing for rapid exchange of air between the environment and the canister; this has no effect on the environment because air simply passes through the canister as it rises. Finally, for intermediate entrainment rates ($\varepsilon \sim m$), convecting clouds cause profiles to both descend and damp. This may be pictured as a canister that is open at the top and has a small hole in the bottom. In this case, the flow of air through the canister is impeded. Since the canister is lifting air faster than the air can pass through it, the environment must subside by mass conservation, leading to descent of profiles. In addition, air picked up from the environment where a profile is maximal can reside in the canister long enough to be deposited where the profile is minimal, and vice versa, leading to a damping of profiles.

Up to this point, we have focused on the transient case in which an initial wind profile is left to evolve under the sole influence of convection. On the other hand, the atmosphere is host to persistent forcings (e.g., as generated by variations in sea surface temperature) that make a study of steady-state responses of interest as well. To this end, we can calculate the steady-state response to a time-independent acceleration of the form $a\cos(mz)$, where a has units of meters per squared second. In particular, we add this forcing to the right-hand side of Eq. (5), set $\delta = \varepsilon$ as before, set the tendency to zero, and seek a solution of the form

$$v = v_0 \cos[m(z + \Delta z)]. \tag{11}$$

The result gives expressions for v_0 and Δz, which are

$$v_0 = \frac{a\tau}{[1 + (m/\varepsilon)^2]^{1/2}} \quad \text{and} \tag{12}$$

$$\Delta z = \frac{1}{m}\arctan(m/\varepsilon). \tag{13}$$

These equations make new predictions for the amplitude and phase of forced wind profiles in the presence of convection as functions of vertical wavenumber and convective entrainment rate. Figure 4 plots the values of v_0/a and the phase Δzm as functions of wavelength and entrainment rate. The ratio v_0/a, which measures the strength of the response to the forcing, is largest for large wavelengths and large entrainment rates and is smallest for small wavelengths and small entrainment rates. The product Δzm, which measures the phase difference between the forcing and the response, is everywhere positive, signifying a response that is shifted down from the forcing. Large wavelengths and large entrainment rates favor a phase shift near zero, while small wavelengths and small entrainment rates favor a phase shift near 90°.

It is interesting to contrast the left panel of Fig. 4, which shows the time scale v_0/a for a steady-state wind profile, with the left panel of Fig. 1, which shows the damping time scale for a transient wind profile. For large entrainment rates and large wavelengths (i.e., $m/\varepsilon \ll 1$), the two time scales are very similar. For small entrainment rates and small wavelengths, however, the steady-state time scale is much smaller than the transient time scale. How can this be? Let us imagine replacing the continuous acceleration a with a sequence of impulses δv spaced in time by δt such that $\delta v/\delta t = a$; in the limit of small δt, this asymptotically approaches a constant acceleration. We can then think of the steady-state solution [Eq. (11)] as constructed from a sequence of sinusoidal impulses that evolve according to Eq. (6). If these

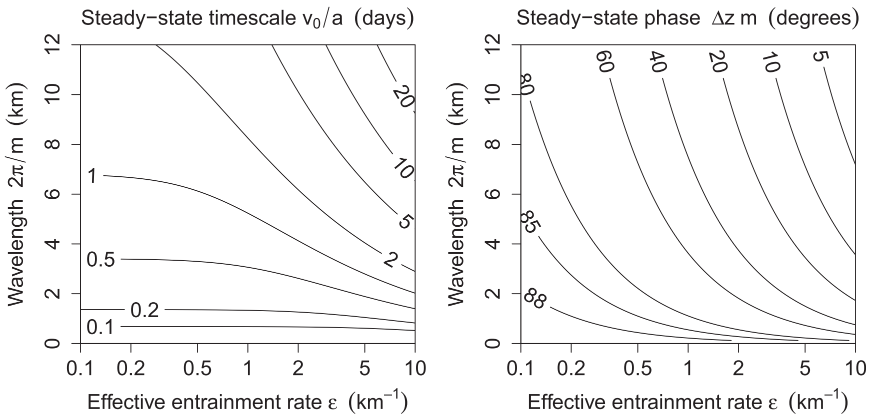

FIG. 4. (left) The amplitude v_0/a and (right) downward phase shift Δzm for steady-state solutions as predicted by Eqs. (12) and (13) using $M/\rho = 1\,\mathrm{cm\,s^{-1}}$.

impulses simply damp in place, as they do for $m/\varepsilon \ll 1$ (i.e., large entrainment rates and large wavelengths), then the transient and steady-state time scales would be identical. But, in addition to decaying, the impulses also descend and, thereby, interfere destructively with impulses applied at earlier and later times. For $m/\varepsilon \gg 1$ (i.e., small entrainment rates and small wavelengths), this destructive interference dominates the response. By this mechanism, convection is able to damp winds very quickly—with a time scale of less than a day—even for small entrainment rates.

3. LES with tracers

We will use large-eddy simulations of steady-state convection to test these theoretical predictions. The cloud-resolving model used for these simulations is Das Atmosphärische Modell (DAM; Romps 2008). The simulations use a doubly periodic domain (38.4 km × 38.4 km × 30 km) with an isotropic grid spacing of 200 m. The lower boundary is a 300-K ocean surface with turbulent enthalpy fluxes given by a bulk aerodynamic formula with a constant drag coefficient of 1.5×10^{-3} and a constant wind speed of $5\,\mathrm{m\,s^{-1}}$. The simulations use interactive shortwave and longwave radiative fluxes calculated using the Rapid Radiative Transfer Model (RRTM; Clough et al. 2005; Iacono et al. 2008) with the top-of-the-atmosphere insolation set to the diurnal average at the equator on 1 January. The Coriolis force is omitted, as is appropriate for circulations on the equator.

To evaluate the predictions of section 2, we begin by studying the evolution of a sinusoidal tracer profile in a deeply convecting atmosphere. For a passive tracer, Eqs. (1)–(3) become

$$\partial_z M = (\varepsilon - \delta)M\,, \tag{14}$$

$$\rho\partial_t q = \partial_z[M(q - q_c)], \quad \text{and} \tag{15}$$

$$\partial_z q_c = \varepsilon(q - q_c)\,, \tag{16}$$

where q_c and q denote the mixing ratio of the passive tracer in the cloud and environment, respectively. The derivation of section 2 applies without alteration to tracers; the relevant equations are obtained by the substitution of q and q_c for v and v_c.

We first run a spinup simulation for several weeks to reach radiative–convective equilibrium. The deep-convective mass flux M in this simulation is characterized by a value of $M/\rho \simeq 1\,\mathrm{cm\,s^{-1}}$, and it is associated with a precipitation rate of about $2\,\mathrm{mm\,day^{-1}}$. We take a 3D snapshot from the end of the spinup simulation and add a passive tracer with q distributed as

$$q(\mathbf{x}) = q_0 \sin(mz)\,,$$

where m is the wavenumber of the profile. The simulation is then restarted from this state and run for 4 more days. This is repeated with nine different values of $m = 2\pi/\lambda$ with wavelengths of $\lambda = 2, 3, \ldots, 10$ km. Wavelengths smaller than 2 km are not considered because they are poorly resolved by a 200-m grid spacing. Wavelengths greater than 10 km are not considered for two reasons: their descent and damping are more difficult to diagnose, and the approximation of $\varepsilon = \delta$ becomes worse as the wavelength increases (see the discussion later in this section).

Figure 5 shows Hovmöller plots of horizontally averaged q for three of these simulations. Time runs from left to right along the abscissa with time beginning at the moment that the simulation is restarted with the sinusoidal tracer profile. Height increases upward along the ordinate, and the colors indicate the horizontal average

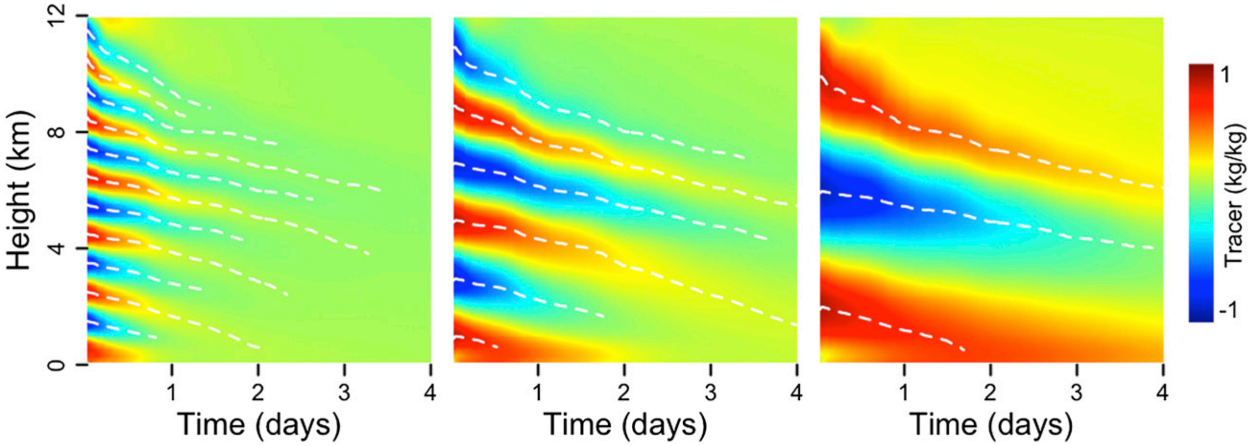

FIG. 5. Hovmöller plots for profiles of passive tracers with wavelengths equal to (left) 2, (middle) 4, and (right) 8 km.

of q. From left to right, the three panels show the results with $\lambda = 2, 4$, and 8 km. To aid the eye, the white dashed lines in Fig. 5 track the temporal evolution of extrema in the mean tracer profile.

Some qualitative features are easily noted from Fig. 5. First, it is clear that the tracer profiles retain their sinusoidal shape in the troposphere but descend (i.e., $w < 0$) as expected from Eq. (9). After 2 days, a sinusoid with a best-fit phase explains 56% of the variance in the 2-km-wavelength profile (despite the fact that the amplitude has all but vanished) and 96% of the variance in the 10-km-wavelength profile. Furthermore, it is clear that the amplitudes of all the tracer profiles damp to zero with time. In fact, it is clear from visual inspection that, at day 4, the amplitude of the 8-km profile is greater than the amplitude of the 4-km profile, which, in turn, is greater than the amplitude of the 2-km profile. This is strong evidence that the damping time scale increases with wavelength, which is in agreement with Eq. (10).

To make a more quantitative comparison with the theory of section 2, we will first need to diagnose an effective entrainment rate from the large-eddy simulation. For this, we use Eq. (16) to obtain

$$\varepsilon = \frac{\partial_z q_c}{q - q_c}, \tag{17}$$

where q_c is the mass-flux-weighted mixing ratio in the cloudy updrafts and q is the mean mixing ratio over the entire domain. Here, we define cloud updrafts as air with a vertical velocity greater than $1\,\mathrm{m\,s^{-1}}$ and a condensate mass fraction greater than $10^{-5}\,\mathrm{kg\,kg^{-1}}$ (Romps and Kuang 2010). Since q_c and q are easily measured in the LES, ε is straightforward to diagnose, in principle. In practice, however, some precautions must be taken. First, we must average over a sufficiently long time to obtain a robust sampling of the convective ensemble. Second, we must average over a sufficiently short time to avoid q and q_c from changing substantially during the averaging period. To satisfy these two criteria, averages are taken over the first 6 h of the simulations (minus the first half hour to allow the clouds to adjust their tracer concentrations). Third, the bulk-plume model assumes that $\partial_z q_c = 0$ when $q - q_c = 0$, which prevents the right-hand side of Eq. (17) from being singular. In reality, convection does not behave exactly like the bulk-plume equations, so the right-hand side, as diagnosed from LES, is generally singular at the roots of $q - q_c$. Since the profile of every tracer is sinusoidal, the profile of ε, as calculated from any one tracer, has singularities. Therefore, we calculate a composite profile of the entrainment rate as follows: defining $\varepsilon^i(z)$ as the entrainment rate from tracer i at height z calculated from Eq. (17), we define the composite $\varepsilon(z)$ as the average of $\varepsilon^i(z)$ over only those i for which $|q^i - q_c^i| > 0.3q_0$. The resulting $\varepsilon(z)$ is shown in Fig. 6 as the thin black line. Between the cloud base (500 m) and 10 km, the fractional entrainment rate lies in the range of about 0.2–0.8 $\mathrm{km^{-1}}$; the average in that height range is 0.4 $\mathrm{km^{-1}}$. The thick red line is the least squares fit of a quadratic function to the curve between 500 m and 10 km; this curve will be used in the analysis that follows. The dotted blue line is the detrainment rate calculated using Eq. (1), where M is the mass flux of cloudy updrafts.

Several approximations were made in section 2 leading up to Eqs. (9) and (10), and we can use the LES results to check them. The first approximation was the implicit assumption that the bulk-plume equations are an adequate description of convection. It is known, for example, that the bulk-plume equations suffer from the assumption of homogeneity within clouds and the environment (Romps 2010; Dawe and Austin 2011a,b). Of

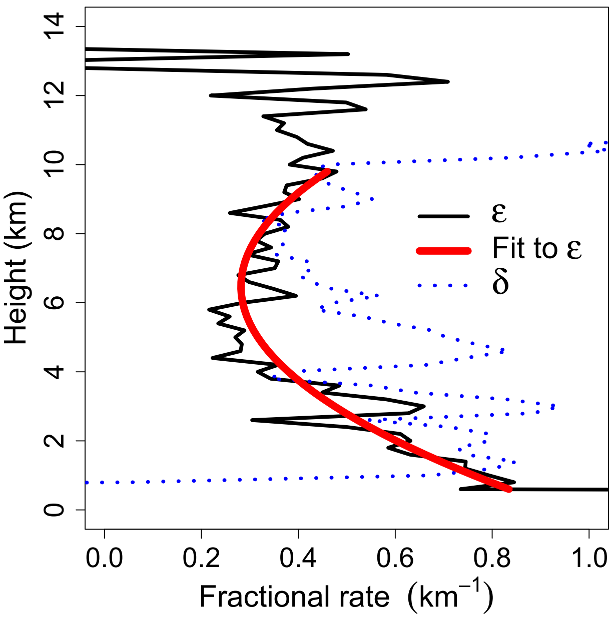

FIG. 6. The entrainment rate (thin black), the quadratic fit to the entrainment rate (thick red), and the detrainment rate (dotted blue) diagnosed from the bulk-plume equations and the tracer simulations.

the bulk-plume equations [Eqs. (14)–(16)], only Eq. (15) provides a testable prediction; Eqs. (14) and (16) simply define the effective ε and δ. In the first column of Fig. 7, the prediction for $\partial_t q$ made by Eq. (15) is shown as the blue curve for the tracers with wavelength 2 (first row), 4 (second row), and 8 km (third row). These predictions for $\partial_t q$ are calculated using values of M, q, and q_c diagnosed directly from the LES. The black curves show the actual tendency of q. Up to a height of 10 km, the agreement between Eq. (15) and the actual $\partial_t q$ is excellent. Above 10 km, deep-convective plumes are detraining, leading to downdrafts from overshooting plumes and clear-air turbulence that are not accounted for in the bulk-plume theory.

Next, we can validate the tracer version (i.e., $\upsilon \to q$) of Eq. (4). Note that there is no υ_c (q_c) in this equation; it gives the tendency in terms of only M, ε, and the profile υ (q). In that equation, δ is not an additional input; it is defined in terms of M and ε via Eq. (1). For this test, $M(z)$ and $q(z)$ are diagnosed as before, and $\varepsilon(z)$ is given by the quadratic fit shown in Fig. 6. The resulting prediction for $\partial_t q$ is shown as the blue curves in the second column of Fig. 7. Once again, the match with the actual tendency, shown by the black curves, is excellent below 10 km. In fact, the result is almost identical to the first column, in which the LES-diagnosed q_c was used. This confirms that the composite entrainment rate in Fig. 6 is correct.

Another approximation used in section 2 is that ε and δ are constant and equal. From glancing at Fig. 6, it would appear that $\varepsilon = \delta$ is a poor approximation. Sometimes, however, looks can be deceiving. To quantify when $\varepsilon = \delta$ qualifies as a "good" approximation, consider Eqs. (7) and (8), which can be Taylor expanded to first order in $\delta - \varepsilon$ to give

$$w = -\frac{M}{\rho}\frac{m^2}{\varepsilon^2 + m^2}\left[1 - \frac{\varepsilon}{m^2}(\delta - \varepsilon)\right] \quad \text{and}$$

$$\tau = \frac{\rho}{M}\frac{\varepsilon^2 + m^2}{\varepsilon m^2}\left[1 - \frac{1}{\varepsilon}(\delta - \varepsilon)\right].$$

These expressions differ from Eqs. (9) and (10) by the extra terms proportional to $\delta - \varepsilon$. Therefore, the approximation of $\varepsilon = \delta$ is good so long as two conditions hold: $|\delta - \varepsilon| \ll m^2/\varepsilon$ and $|\delta - \varepsilon| \ll \varepsilon$. Note that the former inequality becomes increasingly stringent as the vertical wavelength of the profile increases; this is one of the reasons why we do not consider wavelengths greater than 10 km. To see if we are in danger of violating these inequalities, let us consider the largest wavelength in this study (i.e., 10 km). With $\varepsilon = 0.4\,\text{km}^{-1}$ (the mean value diagnosed from Fig. 6), these conditions require that $|\delta - \varepsilon|$ be smaller than $m^2/\varepsilon = 1.0\,\text{km}^{-1}$ and $\varepsilon = 0.4\,\text{km}^{-1}$. With the exception of the melting line, where δ exceeds ε by as much as $0.6\,\text{km}^{-1}$, these conditions are obeyed. Therefore, it is reasonable to make the approximation of $\varepsilon = \delta$.

As for the approximation of constant ε and δ, the most direct way to assess this is to evaluate the resulting prediction for $\partial_t q$. The third column of Fig. 7 shows the prediction from Eq. (4) with $\varepsilon = \delta = 0.4\,\text{km}^{-1}$. The quality of the match between the theory and the LES has degraded somewhat, and this appears to be due to the inconsistency generated by the simultaneous use of $\varepsilon = \delta$ (which would imply constant M) and the actual height-dependent M. This is largely remedied by replacing M/ρ with its mean value of $0.9\,\text{cm}\,\text{s}^{-1}$ between cloud base and 10 km. As shown in the fourth column of Fig. 7, this significantly improves the agreement with the LES below 10 km, although it leads to erroneous predictions in the stratosphere, where there is no convection. These results confirm the appropriateness of the approximations made in section 2.

Finally, we can directly compare damping and descent rates in the LES to the predictions made by Eqs. (9) and (10). The descent speed is calculated as the change in Δz over the 5.5 h, where Δz is the distance that gives the best correlation between $\sin[m(z + \Delta z)]$ and the q profile of wavenumber m for $z \in [0.5, 10]$ km. The damping time scale is calculated as 5.5 h divided by the fractional

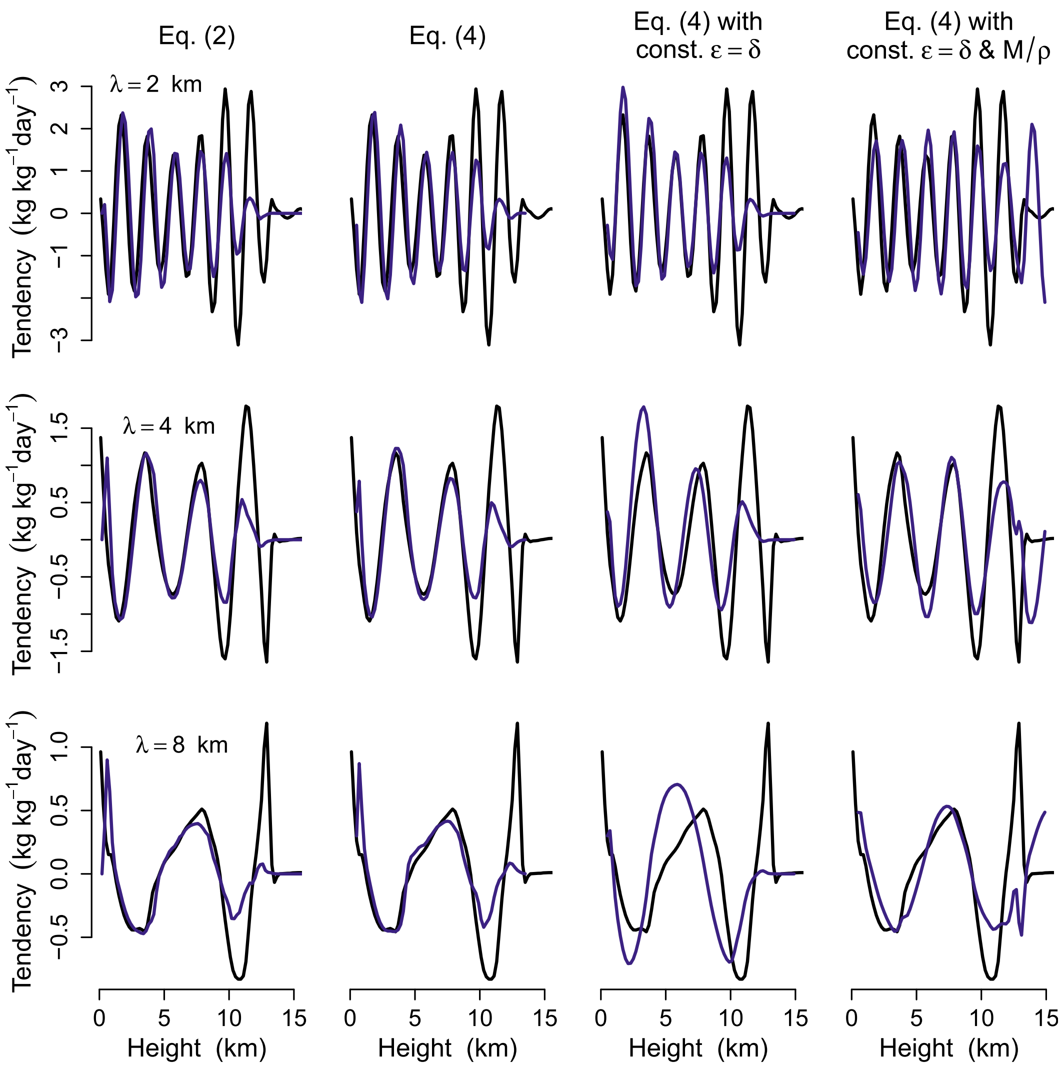

FIG. 7. Validation of Eqs. (2) and (4), and of the approximations of constant $\varepsilon = \delta$ and constant M/ρ. The black curve plots the actual $\partial_t v$ of the tracer in the LES with wavelength equal to (top) 2, (middle) 4, and (bottom) 8 km. The blue curve plots the prediction for $\partial_t v$ given by (first column) Eq. (2), (second column) Eq. (4) using the parabolic fit to ε, (third column) Eq. (4) using a constant $\varepsilon = \delta = 0.4\,\mathrm{km}^{-1}$, and (fourth column) Eq. (4) using a constant $\varepsilon = \delta$ and a constant M/ρ.

change in the integral from 0.5 to 10 km of $\sin[m(z + \Delta z)]$ times q. (Nearly identical damping time scales are obtained by using the fractional change in the integral of $|q|$.) These results are plotted as the connected circles in Fig. 8. Equations (9) and (10) are plotted as the solid curves using the values of $M/\rho = 0.9\,\mathrm{cm\,s}^{-1}$ and $\varepsilon = 0.4\,\mathrm{km}^{-1}$ diagnosed from the LES. We see that the theory successfully predicts the order of magnitude of the damping time scale and descent speed, and it correctly predicts an increase in damping time scale and a decrease in descent speed with wavelength. Of course, the quantitative agreement in Fig. 8 is certainly not perfect, and this is to be expected given the many approximations used in section 2 to arrive at an analytical theory. The sensitivity to the integration time can be tested by using, in place of 5.5 h, integration times as small as 1.5 h and as large as 2 days, both of which yield similar results. In addition, similar agreement between the LES and theory is obtained by tracking the decay and descent of individual extrema in the profiles, although this makes the LES results noisier.

4. LES with wind

These results have been for passive tracers, but what about wind? Since the pressure gradient force has been

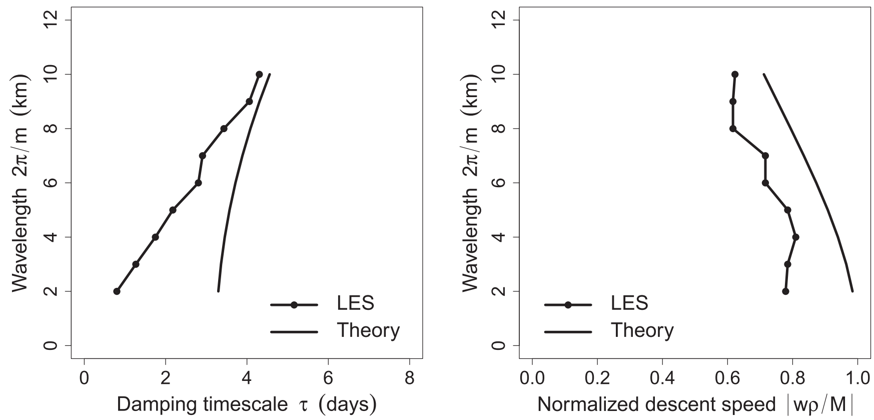

FIG. 8. (left) Damping time scale and (right) descent speed for sinusoidal tracer profiles as functions of wavelength as calculated from the LES (circles) and from the theory (solid curve). The theoretical predictions are calculated from Eq. (10) for the left panel and Eq. (9) for the right panel using $M/\rho = 0.9\,\mathrm{cm\,s^{-1}}$ and $\varepsilon = 0.4\,\mathrm{km^{-1}}$.

folded into an effective entrainment in the derivation of Eqs. (9) and (10), it is not clear a priori how successful these equations might be in predicting the evolution of wind profiles. To test this, we take a 3D snapshot from the end of the spinup simulation and add a sinusoidal perturbation to the y component of the wind,

$$v(\mathbf{x}) \rightarrow v'(\mathbf{x}) = v(\mathbf{x}) - \overline{v}(z) + v_0 \sin(mz),$$

where an overbar denotes an average over x and y, and $v_0 = 1\,\mathrm{m\,s^{-1}}$. This replaces the mean wind profile $\overline{v}(z)$ with a sinusoidal wind profile $v_0 \sin(mz)$ without affecting the cloud-scale circulations. The simulation is then run for 4 days of model time, and this experiment is repeated nine times for vertical wavelengths ranging from 2 to 10 km in 1-km increments.

Since the applied wind profiles have a small amplitude, the strength, depth, and organization of the convection is largely unaffected by the different wind profiles. Therefore, we can interpret these simulations as the same state of convection operating on nine different wind profiles. Figure 9 shows the Hovmöller plot for the wind profiles with wavelengths equal to 2, 4, and 8 km. As with the tracers, the wind profiles retain their sinusoidal shape while descending in the troposphere. After 2 days, a sinusoid with a best-fit phase explains 56% of the variance in the 2-km-wavelength profile and 97% of the variance in the 10-km-wavelength profile. Furthermore, it is clear that the damping rate and descent speed both decrease as wavelength increases, as predicted by the theory in section 2. To be more quantitative, however, we will need to repeat the analysis of the previous section.

Since, for wind, the effective entrainment describes the combined effects of entrainment and pressure, we should expect to diagnose a larger entrainment rate from

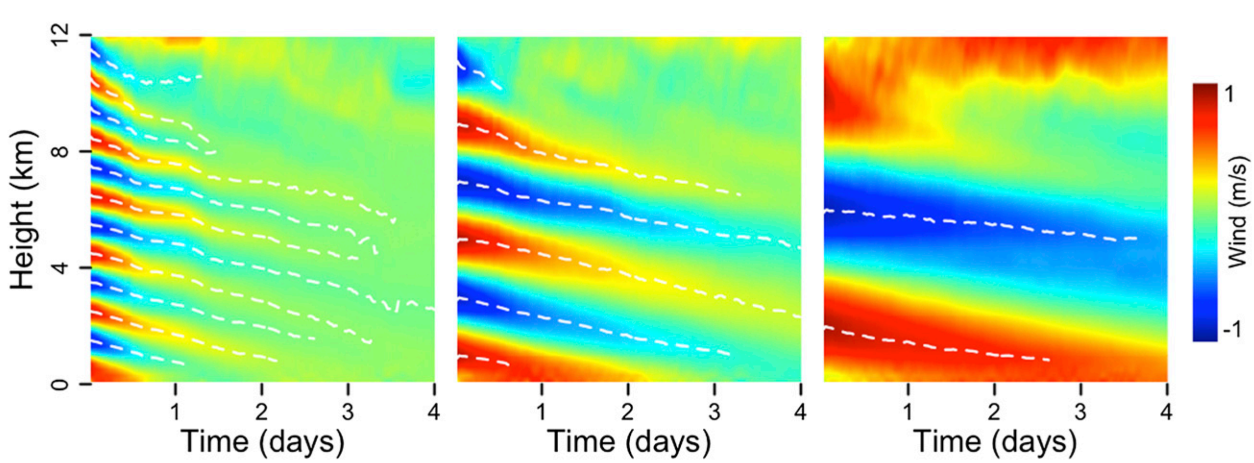

FIG. 9. As in Fig. 5, but for wind.

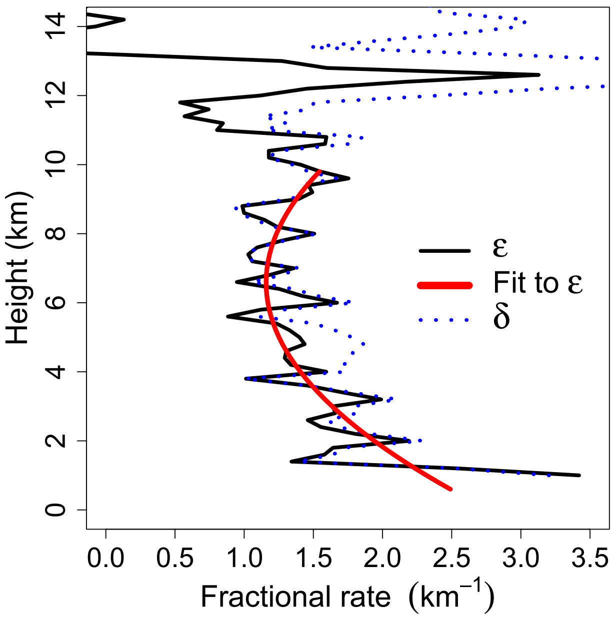

FIG. 10. As in Fig. 6, but for wind.

$$\varepsilon = \frac{\partial_z v_c}{v - v_c} \tag{18}$$

than we obtained with passive tracers in Eq. (17). As in the previous section, means are taken from the first 6 h (minus the first half hour to allow the clouds to adjust their horizontal winds). Constructing a composite entrainment profile from Eq. (18), we obtain the entrainment rate shown in Fig. 10. The entrainment rate is significantly larger than that in Fig. 6, with the profile mostly exceeding 1 km^{-1} between cloud base and 10 km. The mean of the entrainment profile between cloud base (500 m) and 10 km is 1.5 km^{-1}, compared with 0.4 km^{-1} for the passive tracers.

As before, $\varepsilon = \delta$ is a good assumption if $|\delta - \varepsilon| \ll m^2/\varepsilon$ and $|\delta - \varepsilon| \ll \varepsilon$. For $\varepsilon = 1.5$ km^{-1}, the former inequality is the more restrictive, requiring $|\delta - \varepsilon| \ll 0.2$ km^{-1} for a wavelength of 10 km. In Fig. 10, it is clear that this is satisfied everywhere between cloud base and 10 km, except near 5 km.

Figures 11 and 12 repeat the analyses of the previous section. In Fig. 11, we see that Eq. (4) does an excellent job of matching the actual tendencies, even with the assumptions of constant M/ρ and constant $\varepsilon = \delta$. Figure 12 compares the damping time scale and descent speeds diagnosed from the LES and predicted by the theory. It is worth repeating that the many approximations used in the derivation of Eqs. (9) and (10) limit their quantitative accuracy. Nonetheless, we see that the theory of section 2 predicts the correct order of magnitude for the damping time scale and descent speed, as well as the increase in damping time scale and decrease in descent speed with increasing wavelength.

5. Summary and discussion

In toy models of atmospheric circulations, Rayleigh damping serves as a convenient sink for free-tropospheric momentum, and its physical origins are usually attributed to moist convection. Rayleigh damping eliminates momentum on a fixed time scale—regardless of the shape of the wind profile—and it does not cause wind profiles to descend. In contrast, the theory developed here predicts that convection causes profiles of mass and momentum to both descend and damp with profile-dependent rates. Profiles dominated by large vertical wavelengths descend and damp slowly, while profiles dominated by small vertical wavelengths descend and damp quickly. This theory is summarized mathematically by Eqs. (9) and (10) for the evolution of unforced wind profiles and by Eqs. (12) and (13) for forced wind profiles.

The theory predicts that the descent speed of mass and wind profiles are always less than or equal to that of compensating subsidence; see Eqs. (7) and (9) and the right panel of Fig. 1. This is confirmed by large-eddy simulations; see the right panels of Figs. 8 and 12. The theory also predicts that the damping time scales for mass and wind profiles with a 2–10-km vertical wavelength are in the ballpark of 1–10 days for rain rates typical of tropical RCE; see the left panel of Fig. 1. This is confirmed by large-eddy simulations; see the left panels of Figs. 8 and 12. Large-eddy simulations also confirm that long vertical wavelengths damp slower (see left panels of Figs. 8 and 12) and descend slower (see right panels of Figs. 8 and 12) than short vertical wavelengths.

A counterintuitive result of this theory is that highly entraining convection has no impact on profiles of tracers or wind. Physically, this occurs because a very large entrainment rate in Eq. (3) forces the cloud properties to be nearly identical to those of the environment (i.e., $\boldsymbol{v} - \boldsymbol{v}_c = 0$ in that equation), and this leads to zero eddy fluxes in Eq. (2). Conceptually, we may think of a highly entraining cloud as an open canister, as pictured in the middle panel of Fig. 3: environmental air passes right through the cloud, leading to neither damping nor descent of environmental profiles. Mathematically, we can see this effect in Eqs. (9) and (10): both the damping rate $1/\tau$ and the descent speed w go to zero as ε goes to infinity.

The analytical theory presented here is derived with the aid of many approximations, including the use of the bulk-plume equations. For the convective transport of horizontal momentum, the pressure gradient force has

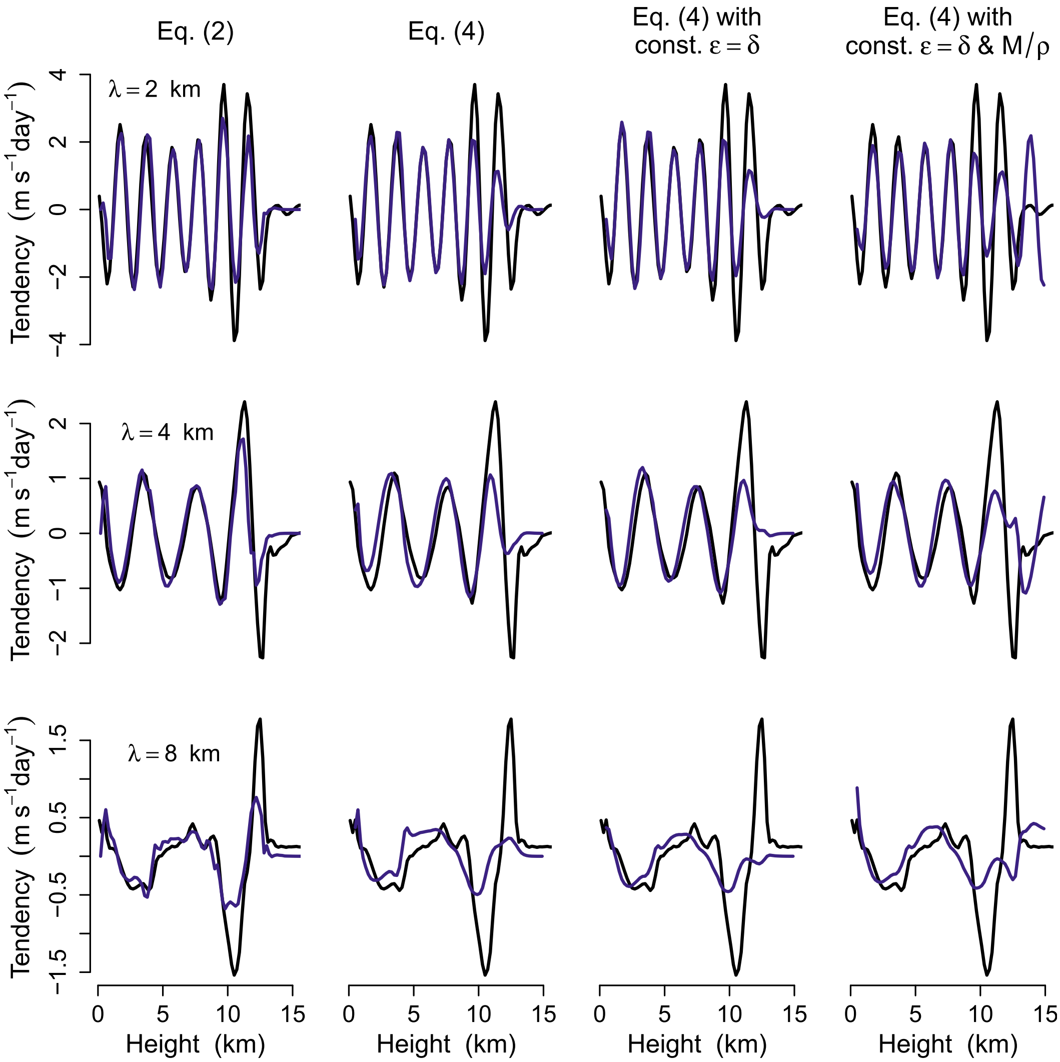

FIG. 11. As in Fig. 7, but for wind, and with $\varepsilon = \delta = 1.5\,\mathrm{km}^{-1}$ in the third and fourth columns.

been approximated here as an effective entrainment. Consequently, the effective entrainment rate diagnosed from the evolution of wind profiles is almost 4 times larger than the entrainment rate diagnosed from the tracer profiles (i.e., $1.5\,\mathrm{km}^{-1}$ compared to $0.4\,\mathrm{km}^{-1}$). This indicates a significant role for the pressure gradient force in convective momentum transport.

In a previous study by Romps (2012b), it was found that narrow jets move vertically at a speed of $-M/\rho$ (i.e., the speed of compensating subsidence). The theory derived here provides an explanation for that behavior. From Eq. (9), we see that the descent speed goes to $-M/\rho$ in the limit of large m. Since Romps (2012b) was injecting momentum in a single vertical layer, that study was operating well within the large-m limit. That study also argued in favor of modeling the pressure gradient force as $F \propto \boldsymbol{v} - \boldsymbol{v}_c$ (i.e., as an effective entrainment) instead of the proposal by Gregory et al. (1997) to model the pressure gradient force as $F \propto \partial_z \boldsymbol{v}$. The success found here in treating pressure as an effective entrainment lends support to the approach, although further study of the pressure gradient force is needed before a definitive formulation can be reached.

The vertical wavelengths studied here range from 2 to 10 km. As discussed in section 3, this range is limited by the inability of the large-eddy simulation to resolve significantly smaller wavelengths and the expected deviations from theory and the difficulty of designing diagnostics for significantly larger wavelengths. Nevertheless, the results obtained for this range of wavelengths are immediately applicable to a variety of problems, including the evolution of the stacked shallow circulations often seen in cloud-resolving simulations of a Walker cell; see, e.g., Fig. 4a of Blossey et al. (2010), the third

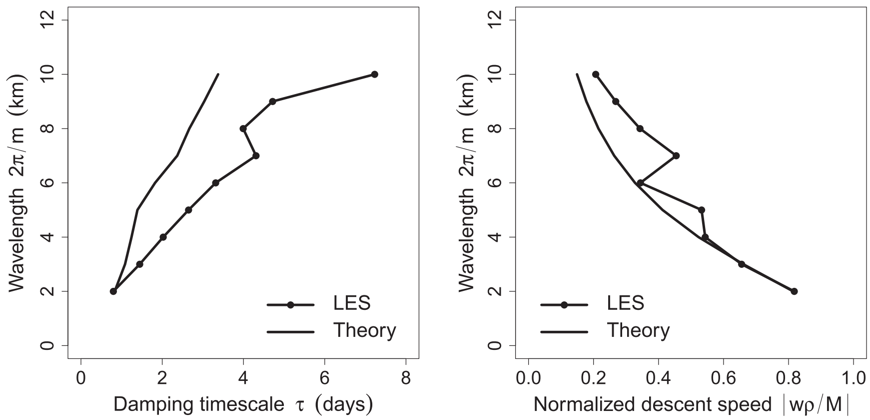

FIG. 12. As in Fig. 8, but for wind.

panel of Fig. 1 in Romps (2012a), Figs. 6c, 7c, and 8c of Grabowski et al. (2000), and Figs. 4b and 5 of Bretherton et al. (2006). It is also hoped that this theory could be used to prescribe the momentum damping in the versions of the weak pressure gradient approximation that use Rayleigh damping (e.g., Raymond and Zeng 2000; Kuang 2008; Blossey et al. 2009; Kuang 2011; Romps 2012c,a).

Acknowledgments. This work was supported by the U.S. Department of Energy's Atmospheric System Research—an Office of Science, Office of Biological and Environmental Research program under Contract DE-AC02-05CH11231. This research used computing resources of the National Energy Research Scientific Computing Center (NERSC), which is supported by the Office of Science of the U.S. Department of Energy under Contract DE-AC02-05CH11231, and computing resources of the Extreme Science and Engineering Discovery Environment (XSEDE), which is supported by National Science Foundation Grant OCI-1053575. The feedback from three anonymous reviewers significantly improved the manuscript.

REFERENCES

Blossey, P. N., C. S. Bretherton, and M. C. Wyant, 2009: Subtropical low cloud response to a warmer climate in a superparameterized climate model. Part II: Column modeling with a cloud resolving model. *J. Adv. Model. Earth Syst.,* **1,** 8, doi:10.3894/JAMES.2009.1.8.

——, Z. Kuang, and D. M. Romps, 2010: Isotopic composition of water in the tropical tropopause layer in cloud-resolving simulations of an idealized tropical circulation. *J. Geophys. Res.,* **115,** D24309, doi:10.1029/2010JD014554.

Bretherton, C. S., P. N. Blossey, and M. E. Peters, 2006: Interpretation of simple and cloud-resolving simulations of moist convection–radiation interaction with a mock-Walker circulation. *Theor. Comput. Fluid Dyn.,* **20,** 421–442.

Carr, M. T., and C. S. Bretherton, 2001: Convective momentum transport over the tropical pacific: Budget estimates. *J. Atmos. Sci.,* **58,** 1673–1693.

Chang, C. P., 1977: Viscous internal gravity waves and low-frequency oscillations in the tropics. *J. Atmos. Sci.,* **34,** 901–910.

——, and H. Lim, 1982: On the effects of viscous damping on equatorial Rossby waves. *J. Atmos. Sci.,* **39,** 1726–1733.

Clayson, C. A., and L. Kantha, 2008: On turbulence and mixing in the free atmosphere inferred from high-resolution soundings. *J. Atmos. Oceanic Technol.,* **25,** 833–852.

Clough, S., M. Shephard, E. Mlawer, J. Delamere, M. Iacono, K. Cady-Pereira, S. Boukabara, and P. Brown, 2005: Atmospheric radiative transfer modeling: A summary of the AER codes. *J. Quant. Spectrosc. Radiat. Transfer,* **91,** 233–244.

Dawe, J. T., and P. H. Austin, 2011a: Interpolation of LES cloud surfaces for use in direct calculations of entrainment and detrainment. *Mon. Wea. Rev.,* **139,** 444–456.

——, and ——, 2011b: The influence of the cloud shell on tracer budget measurements of LES cloud entrainment. *J. Atmos. Sci.,* **68,** 2909–2920.

Gill, A. E., 1980: Some simple solutions for heat-induced tropical circulation. *Quart. J. Roy. Meteor. Soc.,* **106,** 447–462.

Grabowski, W. W., J.-I. Yano, and M. W. Moncrieff, 2000: Cloud resolving modeling of tropical circulations driven by large-scale SST gradients. *J. Atmos. Sci.,* **57,** 2022–2040.

Gregory, D., R. Kershaw, and P. M. Inness, 1997: Parametrization of momentum transport by convection. II: Tests in single-column and general circulation models. *Quart. J. Roy. Meteor. Soc.,* **123,** 1153–1183.

Holton, J. R., and D. E. Colton, 1972: A diagnostic study of the vorticity balance at 200 mb in the tropics during the northern summer. *J. Atmos. Sci.,* **29,** 1124–1128.

Houze, R., 1973: A climatological study of vertical transports by cumulus-scale convection. *J. Atmos. Sci.,* **30,** 1112–1123.

Iacono, M., J. Delamere, E. Mlawer, M. Shephard, S. Clough, and W. Collins, 2008: Radiative forcing by long-lived greenhouse gases: Calculations with the AER radiative transfer models. *J. Geophys. Res.,* **113,** D13103, doi:10.1029/2008JD009944.

Johnson, R. H., 1976: The role of convective-scale precipitation downdrafts in cumulus and synoptic-scale interactions. *J. Atmos. Sci.,* **33,** 1890–1910.

Jorgensen, D., E. Zipser, and M. LeMone, 1985: Vertical motions in intense hurricanes. *J. Atmos. Sci.,* **42,** 839–856.

Kuang, Z., 2008: Modeling the interaction between cumulus convection and linear gravity waves using a limited-domain cloud system–resolving model. *J. Atmos. Sci.,* **65,** 576–591.

——, 2011: The wavelength dependence of the gross moist stability and the scale selection in the instability of column-integrated moist static energy. *J. Atmos. Sci.,* **68,** 61–74.

Lee, S.-K., C. Wang, and B. E. Mapes, 2009: A simple atmospheric model of the local and teleconnection responses to tropical heating anomalies. *J. Climate,* **22,** 272–284.

LeMone, M. A., 1983: Momentum transport by a line of cumulonimbus. *J. Atmos. Sci.,* **40,** 1815–1834.

Lin, J. L., M. Zhang, and B. Mapes, 2005: Zonal momentum budget of the Madden–Julian oscillation: The source and strength of equivalent linear damping. *J. Atmos. Sci.,* **62,** 2172–2188.

——, B. E. Mapes, and W. Han, 2008: What are the sources of mechanical damping in Matsuno–Gill-type models? *J. Climate,* **21,** 165–179.

Malkus, J. S., 1952: The slopes of cumulus clouds in relation to external wind shear. *Quart. J. Roy. Meteor. Soc.,* **78,** 530–542.

Mapes, B. E., and X. Wu, 2001: Convective eddy momentum tendencies in long cloud-resolving model simulations. *J. Atmos. Sci.,* **58,** 517–526.

Matsuno, T., 1966: Quasi-geostrophic motions in the equatorial area. *J. Meteor. Soc. Japan,* **44,** 25–43.

Moncrieff, M. W., 1992: Organized convective systems: Archetypal dynamical models, mass and momentum flux theory, and parametrization. *Quart. J. Roy. Meteor. Soc.,* **118,** 819–850.

Neelin, J. D., I. M. Held, and K. H. Cook, 1987: Evaporation-wind feedback and low-frequency variability in the tropical atmosphere. *J. Atmos. Sci.,* **44,** 2341–2348.

Raymond, D. J., and X. Zeng, 2000: Instability and large-scale circulations in a two-column model of the tropical troposphere. *Quart. J. Roy. Meteor. Soc.,* **126,** 3117–3135.

Robe, F. R., and K. A. Emanuel, 2001: The effect of vertical wind shear on radiative–convective equilibrium states. *J. Atmos. Sci.,* **58,** 1427–1445.

Romps, D. M., 2008: The dry-entropy budget of a moist atmosphere. *J. Atmos. Sci.,* **65,** 3779–3799.

——, 2010: A direct measure of entrainment. *J. Atmos. Sci.,* **67,** 1908–1927.

——, 2012a: Numerical tests of the weak pressure gradient approximation. *J. Atmos. Sci.,* **69,** 2846–2856.

——, 2012b: On the equivalence of two schemes for convective momentum transport. *J. Atmos. Sci.,* **69,** 3491–3500.

——, 2012c: Weak pressure gradient approximation and its analytical solutions. *J. Atmos. Sci.,* **69,** 2835–2845.

——, and Z. Kuang, 2010: Do undiluted convective plumes exist in the upper tropical troposphere? *J. Atmos. Sci.,* **67,** 468–484.

Schneider, E. K., and R. S. Lindzen, 1976: A discussion of the parameterization of momentum exchange by cumulus convection. *J. Geophys. Res.,* **81,** 3158–3160.

——, and ——, 1977: Axially symmetric steady-state models of the basic state for instability and climate studies. Part I. Linearized calculations. *J. Atmos. Sci.,* **34,** 263–279.

Seager, R., 1991: A simple model of the climatology and variability of the low-level wind field in the tropics. *J. Climate,* **4,** 164–179.

Sugiyama, M., 2009: The moisture mode in the quasi-equilibrium tropical circulation model. Part II: Nonlinear behavior on an equatorial β plane. *J. Atmos. Sci.,* **66,** 1525–1542.

Wilson, R., 2004: Turbulent diffusivity in the free atmosphere inferred from MST radar measurements: A review. *Ann. Geophys.,* **22,** 3869–3887.

Wu, X., and M. Yanai, 1994: Effects of vertical wind shear on the cumulus transport of momentum: Observations and parameterization. *J. Atmos. Sci.,* **51,** 1640–1660.

Wu, Z., D. S. Battisti, and E. S. Sarachik, 2000: Rayleigh friction, Newtonian cooling, and the linear response to steady tropical heating. *J. Atmos. Sci.,* **57,** 1937–1957.

Yang, W., R. Seager, and M. A. Cane, 2013: Zonal momentum balance in the tropical atmospheric circulation during the global monsoon mature months. *J. Atmos. Sci.,* **70,** 583–599.

Yu, J. Y., and J. D. Neelin, 1997: Analytic approximations for moist convectively adjusted regions. *J. Atmos. Sci.,* **54,** 1054–1063.